A probabilistic segmentation method for the identification of luminal borders in intravascular ultrasound images

Gerardo Mendizabal-Ruiz[1,2], Mariano Rivera[1] and Ioannis A. Kakadiaris[2]

[1] Centro de Investigación en Matemáticas. (*http://www.cimat.mx*)

[2] Computational Biomedicine Laboratory, University of Houston. (*http://www.cbl.uh.edu*)

Abstract

Intravascular ultrasound (IVUS) is a catheter-based medical imaging technique that produces cross-sectional images of blood vessels and is particularly useful for studying atherosclerosis. In this paper, we present a probabilistic approach for the semi-automatic identification of the luminal border on IVUS images. Specifically, we parameterize the lumen contour using a mixture of Gaussian that is deformed by the minimization of a cost function formulated using a probabilistic approach. For the optimization of the cost function, we introduce a novel method that linearly combines the descent directions of the steepest descent and BFGS optimization methods within a trust region that improves convergence. Results of our proposed method on 20 MHz IVUS images are presented and discussed in order to demonstrate the effectiveness of our approach.

1. Introduction

Complications attributed to cardiovascular disease (CVD) are currently the main cause of death worldwide. It is known that the majority of adverse CVD-related events are due to coronary artery disease: a condition in which fatty lesions called plaques are formed on the walls of the vessels.

Intravascular ultrasound (IVUS) is an invasive imaging technique capable of providing high-resolution, cross-sectional images of the interior of blood vessels in real time; this allows the collection of morphological information of the vessel and the plaque. Segmentation of IVUS images refers to the delineation of the lumen/intima and media/adventita borders. This process is necessary for assessing the vessel and plaque characteristics [13].

Given that IVUS sequences may be hundreds to thousands of frames long, the manual segmentation of a complete sequence is prohibitively time-consuming. Thus, an automatic segmentation method for IVUS images is needed.

In this paper, we present a method for semi-automatic segmentation of the lumen contour on IVUS images and video sequences. Our contributions are: 1) a probabilistic approach to the segmentation problem that introduces a new parameterization of the lumen contour using a mixture of Gaussians, this contour is deformed by the minimization of a cost function formulated using Markov-random field models with a Bayesian approach inspired by the segmentation method proposed by Rivera *et al*. [14] and Kim *et al*. [8]; 2) a novel minimization method that linearly combines the descent directions of the *steepest descent* and *BFGS* optimization methods within a trust region that stabilizes the convergence; and 3) a multi-scale approach that increases considerably the speed of convergence.

The rest of the paper is organized as follow: Section 2 presents previous work in IVUS segmentation while section 3 presents the methods for our segmentation method. Section 4 presents the results obtained with our method and section 5 presents our conclusions.

2. Previous work

A number of segmentation techniques have been developed for IVUS image analysis. The majority of these methods are based on local properties of image pixels, (e.g. gradient based active surfaces [9] and pixel intensity combined with gradient active contours [10]). Graph search was also investigated using local pixel features and gradient associated to line patterns correlation [18, 19].

Another set of methods was based on global region information (e.g. texture-based morphological processing [11]). Grey-level variances were then used for the optimization of a maximum *a posteriori* (MAP) estimator modeling ultrasound speckle and contour geometry [7].

In other methods, contour detection is accomplished by minimization of a cost function. Sonka *et al*. [15] implemented a knowledge-based graph searching method that incorporates *a priori* knowledge of the artery anatomy and a selected region of interest prior to the automatic border detection. Brusseau *et al*. [2] presented an automatic method for detecting the luminal border based on an active contour

978-1-4244-2243-2/08/$25.00 ©2008 IEEE

that evolves until it optimally separates regions with different statistical properties.

Gil *et al*. [5] introduced a probabilistic segmentation method that deforms a user-provided ellipse model that is initialized close to the artery wall. Later, the same authors [4] proposed a statistical method that involves preprocessing, supervised classification techniques and snakes for segmentation of the media/adventitia contour.

Recently, Unal *et al*. [17] introduced a shape-driven approach to segmentation of the arterial wall from IVUS images. A shape space is obtained by principal component analysis on a training set and then any contour is described as a weighted linear combination of the first k eigenshapes for which the weights are found by the minimization of a energy function.

Previous IVUS image segmentation methods are almost always hampered by noise and artifacts presented on the IVUS images. Although active shape models have been shown to be robust to this problem, a training phase is required to provide the statistical knowledge of the images. Having a training set that is sufficiently representative of all possible IVUS images is a difficult task due to the different shapes that the vessels can take and the variability of the IVUS catheters. In these cases an IVUS image that is dissimilar in shape to those on the training set will be very difficult to segment.

In summary, previous techniques have been hampered by IVUS artifacts, and those that have shown better performance require a prior training phase. Next, we present a probabilistic approach for segmentation of the luminal border of IVUS images that does not require training and that is robust to artifacts.

3. Methods

Similarly to [17], we employ a B-mode polar IVUS image representation. This choice makes the computations much simpler due to the 1D appearance of the interfaces to be detected (Fig. 1). Thus, in the IVUS image domain $\Omega \in \Re^2$, we define the grey-level pixel intensity as $I(x)$ for a pixel with coordinates $x = (\theta, r)$ where $(\theta, r) \in \Omega$ are the angle and radius of the IVUS image respectively (Fig. 2). In this domain, we parameterize the lumen contour as a function $f(\theta, C)$ that depends on the angle and the parameters C.

For the lumen contour to be a smooth periodic curve, we propose modeling it as a periodic mixture of Gaussians. Although our method admits other parametric curves, we have chosen a radial basis function formulation due to the simplicity of the computations. Then, the smoothness of the lumen contour can be controlled by the number of Gaussians and their standard deviations. To reduce the computational cost, we have decided to fix the number of Gaussians N and use the same standard deviation σ for all the Gaussians. Therefore, the lumen contour $f(\theta, C)$ with parameters $C = \{C_0, C_1, ..., C_N\}$ for an IVUS image with width w is given by:

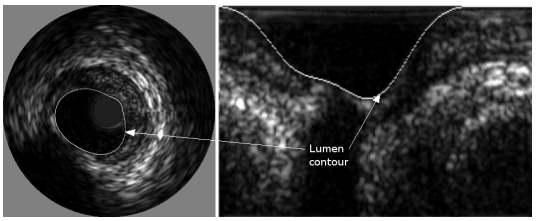

Figure 1. Lumen contour in Cartesian (left) and polar (right) B-mode representations.

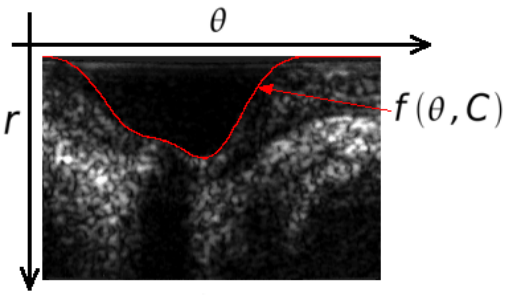

Figure 2. Contour function on rectangular image domain.

$$f(\theta, C) = C_0^2 + \sum_{i=1}^{N} C_i^2 \exp(-\frac{1}{2\sigma^2}(\theta - \mu_i)^2) + \sum_{i=1}^{N} C_i^2 \exp(-\frac{1}{2\sigma^2}(\theta + (w-1) - \mu_i)^2) + \sum_{i=1}^{N} C_i^2 \exp(-\frac{1}{2\sigma^2}(\theta - (w-1) - \mu_i)^2) \,,$$

where C_0 is an offset value to move the curve without changing its shape and $C_i (\forall i \neq 0)$ controls the contribution of the Gaussian i with mean μ_i to the curve.

Since the contour delineates the luminal border and due to the concentric layers morphology of the vessel we can assume that all the pixels inside this contour would correspond to lumen while the pixels outside this contour would correspond to non-lumen. The class for each pixel in the image can be determined using the signed distance function: $g(x, C) = f(\theta, C) - r$, where the pixels with positive values will correspond to lumen, and those with negative values to non-lumen. Since our approach is iterative, while deforming the curve to find the luminal border, we are uncertain about the class of those pixels in the proximity of the contour. Thus, we use a sigmoid function to define the probability $P(x)$ of each pixel x to belong to the class lumen depending on its distance to the curve as follows:

$$P(x) = \frac{1}{1 + e^{-\lambda(f(\theta,C)-r)}} \,.$$

Using this formulation the pixels far above the contour will have a probability close to one for belonging to lumen, while the pixels far below the contour will have probability close to zero. For the pixels near the contour, depending on the value of λ and their distance to the contour, the probability of these pixels belonging to lumen will be around $\frac{1}{2}$ For our binary segmentation case, the probability of a pixel belonging to the class non-lumen is given by $(1 - P(x))$.

Inspired by the Bayesian formulation for image segmentation proposed by Rivera *et al.* [14], we propose the cost function:

$$U(C) = \sum_x P(x, C)d_1(x) + (1 - P(x, C))d_2(x) \; .$$

The functions d_1 and d_2 are defined as $d_k(x) = -log(v_k(x, \phi_k))$, where $v_k(x, \phi_k)$ is the normalized likelihood of the pixel x to be generated by a model k with parameters ϕ_k.

We use the grey-level information (i.e., normalized histograms) to estimate the likelihood of each pixel to belong to the class lumen or the class non-lumen. To estimate these distributions, the user provides samples in the form of a binary map over the IVUS image (Fig. 3(a)). Then, the histograms of regions corresponding to lumen h_1 and non-lumen h_2 are computed using 50 bins and then normalized (Fig. 3(b)). We obtain the likelihoods v_{in} and v_{out} by using the value of the pixel grey-level $I(x)$ on the normalized histogram:

$$v_{in}(x) = \frac{h_{in}(I(x)) + \varepsilon}{h_1(I(x)) + h_2(I(x)) + 2\varepsilon}, \; v_{out}(x) = 1 - v_{in}(x) \; , \tag{1}$$

where ε is a small constant. The likelihood for lumen (Fig. 4(a)) and non-lumen (Fig. 4(b)) are then used for computing the distances d_1 and d_2.

3.1. Optimization method

A number of numerical methods exist for finding the minimum of a cost function; one of the simplest ways is to use a steepest descent method. However, this approach could take a large number of iterations to converge to the solution. Another possibility is to use the Quasi-Newton BFGS method [12]. This method uses second order information to find the optimal descent direction. However, since it is possible to find regions beyond the luminal border that have grey-level distribution similar to lumen, a large step in the optimization could lead to a different local minimal and hence an incorrect segmentation.

Thus, we propose an optimization method that uses a linear combination of the descent directions from steepest descent (p^G) and BFGS (p^{BFGS}) methods within a trust-region (similar to the dogleg method [12]). We will refer to this method as **G+BFGS optimization**.

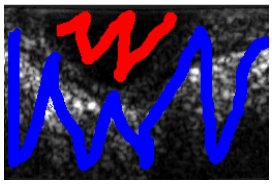

(a)

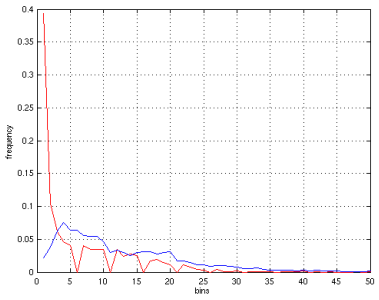

(b)

Figure 3. (a) Binary map created by the user with samples of the lumen and non-lumen. (b) Normalized histogram of the intensities in the two classes.

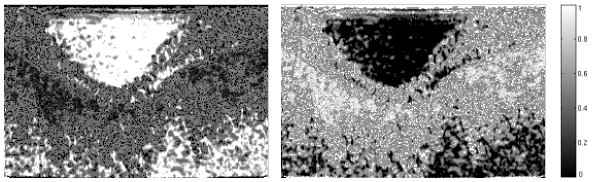

(a) (b)

Figure 4. Depiction of (a) the lumen likelihood and (b) the non-lumen likelihood.

In the BFGS method, the descent direction for each step is computed using $p_k^{BFGS} = -H_k \nabla f_k$, where H_k is an approximation to the Hessian that is updated on each iteration k by: $H_{k+1} = (I - \rho_k s_k y_k^T) H_k (I - \rho_k y_k s_k^T) + \rho_k s_k s_k^T$, with $\rho_k = \frac{1}{y_k^T s_k}$, $s_k = x_{k+1} - x_k$, and $y_k = \nabla f_{k+1} - \nabla f_k$. However, this method establishes a curvature condition that is given by: $s_k^T y_k > 0$. When $s_k^t y_k$ is greater than zero, the curvature of the function becomes more positive as the descent approaches a minimal. If $s_k^t y_k < 0$, the curvature condition is not satisfied and a better descent direction is the negative gradient (i.e., steepest descent direction). Additionally, we note that for small values of $s_k^t y_k$, the computation of the update formula for the Hessian (or its inverse) is undefined.

By design, the more positive the value of ρ, the better the step direction will be. Thus, the contribution of the BFGS descent direction p_k^{BFGS} will be small when ρ is small (preferring steepest descent direction p_k^G). On the other hand, if the value of ρ is more positive, we want to take the BFGS descent direction p_k^{BFGS}. Based on this

analysis, we propose to compute the descent direction as a linear combination of both descent directions: $p_{k+1}^{G+BFGS} = -[\psi(\rho_k)H_k\nabla f_k + (1-\psi(\rho_k))\nabla f_k]$, where the function that controls the contribution of each descent direction $\psi(\rho)$ is defined as:

$$\psi(\rho) = \begin{cases} 0 & \text{if } \rho < 0 \\ \frac{\rho^2}{K+\rho^2} & \text{otherwise} \end{cases} \quad (2)$$

for a constant value of K.

Although the problem with the curvature condition is solved using this linear combination, when using BFGS, if in some step the value of the inner product of $y_k^T s_k$ is very small (but positive) then the value of ρ becomes big and therefore H_{k+1} becomes very big (even when the computed step size α satisfies the Wolfe conditions [12]), making the step too big. This is undesirable because a big step could lead to an incorrect segmentation moving the lumen contour to a region with grey-level profile similar to that of the lumen. To solve this problem, we propose to restrict our proposed descent direction magnitude within a trust region controlled by a fixed parameter T. Thus, after obtaining p_k^{G+BFGS}, the descent direction is normalized:

$$\hat{p}_k^{G+BFGS} = \frac{p_k^{G+BFGS}}{\|p_k^{G+BFGS}\|},$$

and the final descent direction is the normalized descent direction $\hat{p}_k^{G+BFGS}$ scaled by a constant trust region parameter T: $P_k^{G+BFGS} = T\hat{p}_k^{G+BFGS}$.

Algorithm 1 G+BFGS optimization

Require: Initial point x_0, trust region value T, and a tolerance ϵ.

Initialize $H_0 = I$
$p_k^{G+BFGS} = -\nabla f(x_0)$
$k = 0$
while $\|\nabla f(x_k)\| > \epsilon$ **do**
  $\hat{p}_k^{G+BFGS} = \frac{p_k^{G+BFGS}}{\|p_k^{G+BFGS}\|}$
  $P_k^{G+BFGS} = T\hat{p}_k^{G+BFGS}$
  Compute the step size α_k to satisfy the Wolfe conditions
  $x_{k+1} = x_k + \alpha P_k^{G+BFGS}$
  $s_k = x_{k+1} - x_k$
  $y_k = \nabla f(x_k + 1) - \nabla f(x_k)$
  $\rho_k = \frac{1}{y_k^T s_k}$
  $H_{k+1} = (I - \rho_k s_k y_k^T) H_k (I - \rho_k y_k s_k^T) + \rho_k s_k s_k^T$
  $p_{k+1}^{G+BFGS} = -[\psi(\rho_k)H_k\nabla f_k + (1-\psi(\rho_k))\nabla f_k]$
  $k = k + 1$
end while

3.2. Multi-Scale segmentation

Since the computation time in our method will depend on the number of Gaussians used to parameterize the lumen contour, in order to accelerate the convergence, we propose a multi-scale approach on which the number of Gaussians N_i is incremented on each of the multi-scale steps i. At the first step of the multi-scale segmentation a small number of Gaussians (e.g., $N_0 = 3$) is used. Once the optimization converges more Gaussians are added and the optimization is repeated again using as initial point for the next step $i+1$ the curve resulting from the previous step i. This process is repeated until a maximum number of Gaussians M is reached. In addition, the value of σ is reduced as the number of Gaussians is incremented.

To get the initial point for the next step C_0^{i+1} (Fig. 5(a)), we adjust the curve resulting from the previous step $y_i(\theta)$ to the lumen contour function with the new number of Gaussians N_{i+1} (Fig. 5(b)) using the least squares method: $C^{i+1} = \min_C \frac{1}{2}[f(\theta, C) - y(\theta)]^2$.

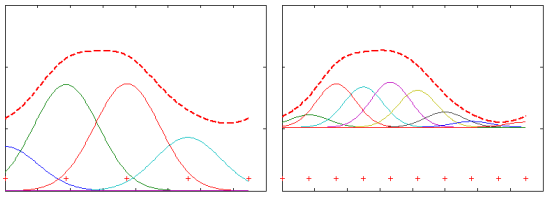

(a) (b)

Figure 5. (a) Lumen contour modeled using 5 Gaussians. (b) Adjustment of the contour in (a) using 10 Gaussians. The + symbol indicates the Gaussian means and the dashed line the lumen contour.

3.3. Single-frame segmentation

For a typical 20MHz IVUS image (Fig. 6(a)), once the histograms and likelihoods are computed from the user-provided map, the segmentation begins with the contour corresponding to the initial point C_0^0. In Fig. 7, we observe that in the first iterations of the first multi-scale step, the lumen contour quickly deforms until it reaches a rough approximation of the luminal border shape. When this step converges, additional Gaussians with a different standard deviation are added to the lumen-contour. In Fig. 8(a) we can observe that at the end of the second step the lumen-contour is starting to look similar to the lumen boundary. On the third step, additional Gaussians are added and at the end of this step the lumen contour is very close to solution (Fig. 8(b)). On the last step, the maximum number of Gaussians is used and the resulting lumen contour is more detailed when compared to the one obtained at the previous step (Fig. 8(c)). Figure 6(b) depicts the segmentation result.

Algorithm 2 Multi-scale segmentation of IVUS images

Require: IVUS image I using polar representation, the number of Gaussians to be used on each multi-scale step $\{N_0, N_1, ..., N_M\}$, the corresponding standard deviations $\{\sigma_0, \sigma_1, ..., \sigma_M\}$ for each multi-scale step, the initial point for the fist step C_0^0 and h_1 and h_2 computed from the map of the luminal area.

1: Compute the normalized histograms h_1 and h_2 from the map.
2: Compute the likelihoods v_{in} and v_{out} using (1).
3: Compute the distances d_1 and d_2.
4: $i = 0$
5: **while** $i \leq M$ **do**
6: Find the lumen contour y_i by solving (3) using the G+BFGS method of algorithm 1.
7: Compute C_0^{i+1} adjusting the curve y_i to the lumen contour function with the number of Gaussians given by N_{i+1}
8: $i = i + 1$
9: **end while**

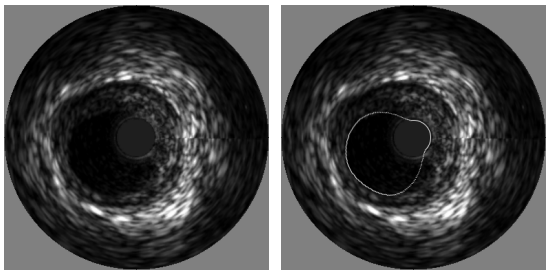

(a) (b)

Figure 6. (a) Depiction of a typical 20 MHz IVUS image to segment and (b) segmentation result.

3.4. Video sequence segmentation

For segmenting an IVUS video sequence, based on the fact that two consecutive IVUS frames have similar luminal grey-level distribution, we use the histogram from the previously segmented frame to compute the likelihoods for the current frame. Similarly, the lumen-contour of the previously segmented frame is used as initial contour for the current frame. For reasons of computational efficiency, only the first frame is segmented starting with a small number of Gaussians; for the segmentation of the consecutive frames we start with the maximum number of Gaussians indicated. Furthermore, it is well known that as the number of samples is increased, the grey-level values class distribution is better estimated by the histogram technique and provides more accurate *a priori* information. We take advantage of this fact by accumulating the histograms of the previously segmented frames from the video sequence and using them on the following frames. This procedure can be seen as a reinforcement learning process. Algorithm 3 presents our approach for semi-automatic segmentation of IVUS video sequences based on our proposed probabilistic segmentation method. Figure 9 depicts the segmentation of four consecutive frames.

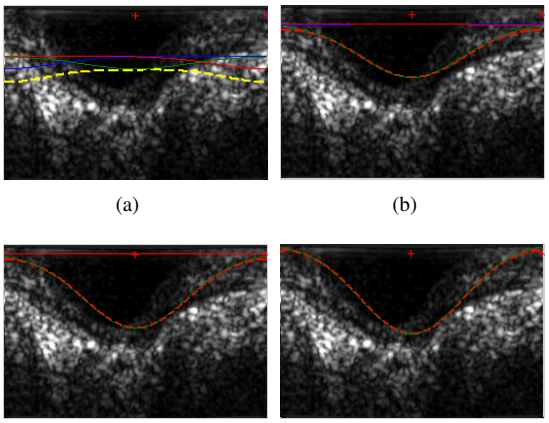

(a) (b)

(c) (d)

Figure 7. Depiction of the deformation of the lumen contour during the first step of the multi-scale method. (a) Initial contour, and after (b-d) 5, 15, and 40 iterations, respectively.

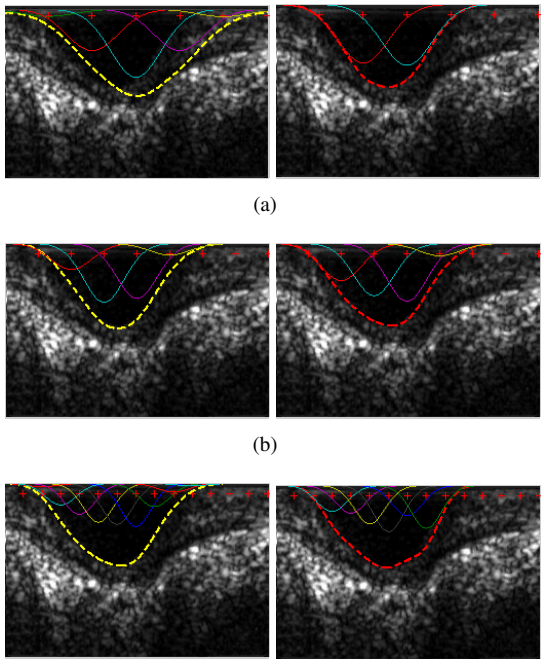

(a)

(b)

(c)

Figure 8. Depiction of the initial (left column) and final (right column) contours for steps 2-4 (a-c, respectively) of the multi-scale segmentation method.

Algorithm 3 IVUS video sequences segmentation

Require: The number of Gaussians to be used on each multi-scale step $\{N_0, N_1, ..., N_M\}$, the corresponding standard deviations for each multi-scale step $\{\sigma_0, \sigma_1, ..., \sigma_M\}$, initial point C_0^0, h_1^0 and h_2^0 computed from the map of the first frame F_0 and the number of frames in the sequence L

1: $H_1 = h_1^0$, $H_2 = h_2^0$.
2: $j = 0$
3: **while** $j < L$ **do**
4: Segment frame F_j with algorithm 2 using H_1 and H_2 as the histograms and initial point C_0^j.
5: Compute h_1^j and h_2^j from the segmented frame F_j
6: $H_1 = H_1 + h_1^j$, $H_2 = H_2 + h_2^j$
7: Obtain C_0^{j+1} using the least squares method with the segmentation result.
8: $j = j + 1$
9: **end while**

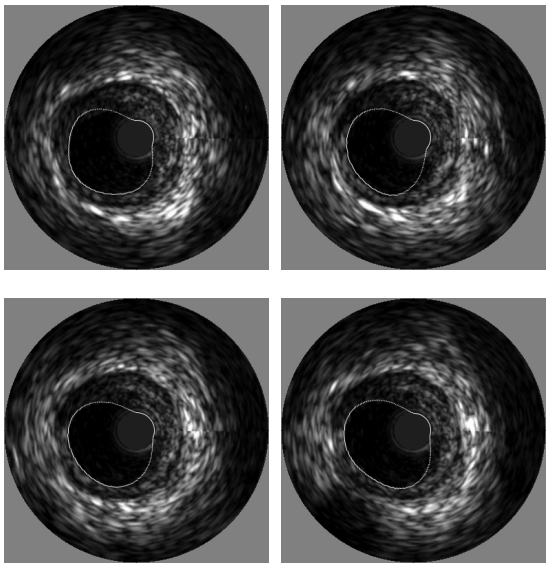

Figure 9. Segmentation of four consecutive frames.

4. Results

The parameters for the generation of the results and how these were selected is discussed next. The uncertainty around the lumen contour is controlled by the sigmoid. We have experimentally selected $\lambda = 0.8$. The initial point C_0^0 for the first step of the multi-scale segmentation should be different from 0 to avoid the trivial solution, we set the offset to be the square root of one quarter of the image height and the rest of the coefficients to be half of the offset. The number of Gaussians and the standard deviation for each of the multi-scale steps will depend on the width of the image and the smoothness we want on the curve. In the fist steps, we are not interested in capturing the details of the luminal border, so a small number of Gaussians with large standard deviation is appropriate. However, on the last steps we are more interested to capture the details of the lumen border. Then, a large number of Gaussians with small standard deviation is required. For our results we have experimentally selected the number of Gaussians to be $\{3, 7, 9, 12\}$ with standard deviations of $\{50, 25, 20, 15\}$ for images with width of 256 pixels. The mean of each Gaussian is selected such that the Gaussians are uniformly distributed into the image width.

We evaluated our method by computing the measures of accuracy recommended by Udupa *et al.* [16]. We compare the automatic segmentation results with manual segmentations on the same image set. For a set of 100 20MHz IVUS images, the mean accuracy was $98.28\% \pm 0.49\%$, the mean true negative rate was $99.43\% \pm 0.29\%$, and the mean true positive rate was $95.57\% \pm 1.69\%$.

The agreement between the areas of the lumen was analyzed using the linear regression analysis and Bland-Altman plots [1]. The inter-observer and automatic (A) mean biases and variabilities for two manual segmentations (MS1 and MS2) for lumen are: the bias of the differences between A and MS1 (A,MS1) was 369.70 ± 336.56; for (A,MS2) the bias was 453.57 ± 304.89 and for (MS1,MS2) was 83.87 ± 343.61. Figure 10 depicts the results of this analysis.

Results on IVUS images with artifacts: Figure 11 depicts the segmentation result on an image with a shadow artifact due to calcified plaque. Although this shadow could be mistakenly interpreted as lumen since it has grey-level intensities similar to the lumen region, we can observe that our segmentation method was able to find the luminal border correctly. Usually the ringdown artifacts are removed by cropping the region that presents this artifact or simply replacing it with some uniform grey-level; however sometimes this artifact is not removed. Since guidewire artifacts are more difficult to remove, they are commonly found on IVUS images. Because this artifact exhibits a bright profile, it can easily be confounded with plaque or other tissue and lead to an incorrect segmentation. Figure 12 depicts the segmentation result on an IVUS image with three artifacts: a ringdown artifact, a small guidewire artifact, and a shadow artifact. Note that none of these artifacts affected the performance of the segmentation.

Figure 13 depicts the segmentation result on an IVUS image with two artifacts: shadow in all the areas beyond the plaque due to calcified plaque, and a larger guidewire than the one on the IVUS image in Fig. 12. Our method was capable of segmenting the image despite the shadow and the guidewire artifact.

Side branches are identified as the opening formed when the vessel being imaged bifurcates. This is visualized as an

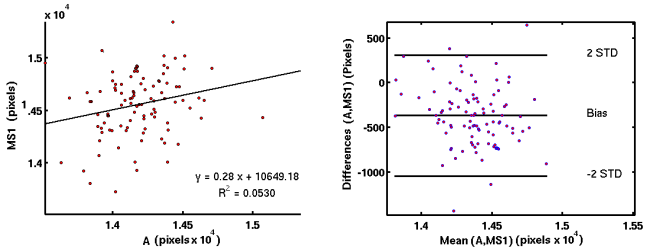

(a)

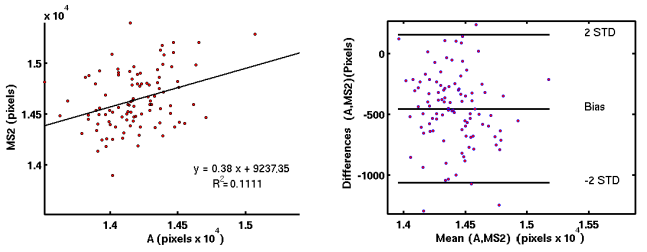

(b)

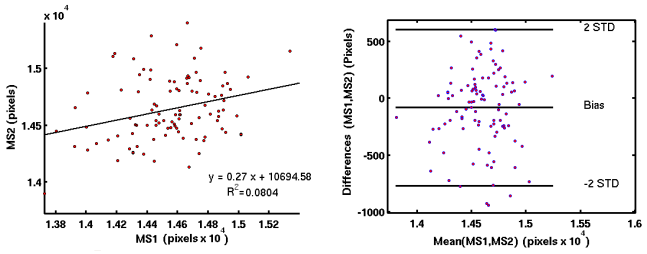

(c)

Figure 10. Bland-Altman plots for lumen segmentation: (a) Automatic vs. Manual segmentation 1, (b) Automatic vs. Manual segmentation 2, (c) Manual segmentation 1 vs. Manual segmentation 2.

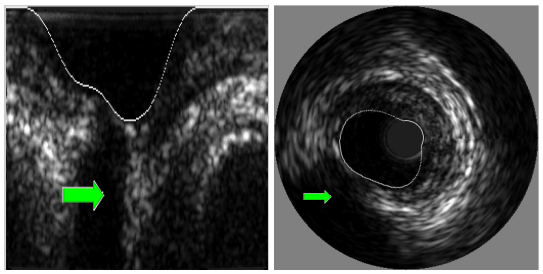

Figure 11. Segmentation example of IVUS image with shadow artifact (the arrow indicates the shadow artifact due to calcified plaque).

.

area of low intensity values extending from the lumen in the near field towards the far field; this represents a challenge for any active-contour based segmentation method because the segmenting contour could advance through this shadow and lead to an incorrect segmentation of the luminal border. Figure 14 depicts the segmentation result on an IVUS image of a relative healthy vessel (i.e., only a small plaque is present) with a side branch. In our method, the smoothness of our lumen contour resolves the problem with branches. However, if we change the smoothness to achieve a better detail, the contour will tend to attempt to segment the side branch as lumen, resulting in an incorrect segmentation.

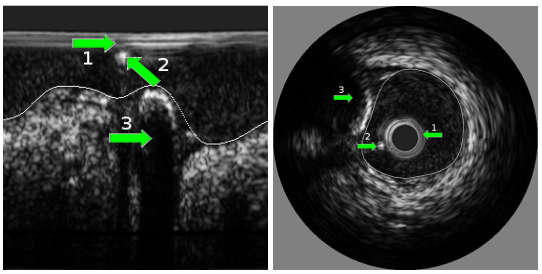

Figure 12. Segmentation example of IVUS image with 1), rigndown artifact, 2) guidewire artifact and 3) shadow artifact.

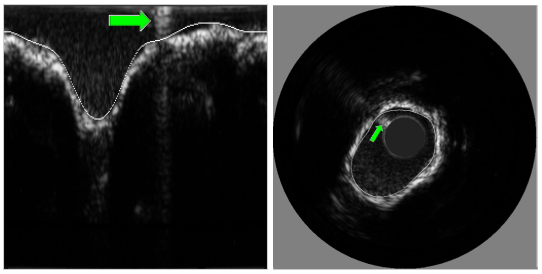

Figure 13. Segmentation example of IVUS image with guidewire artifact: segmentation result.

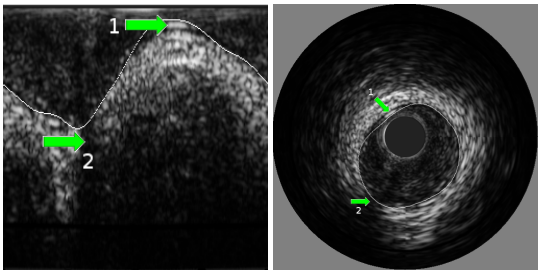

Figure 14. Segmentation example of IVUS image with side branch (indicated by arrow 2) and a small plaque (indicated by arrow 1).

5. Conclusion

We have presented a probabilistic semi-automatic segmentation method for lumen segmentation of IVUS images that is robust to artifacts and that does not require prior training. Our proposed G+BFGS optimization has shown to be an ideal method for this kind of problem because it is faster than the steepest descent optimization and at the same time it can be controlled to avoid big steps that lead to an incorrect segmentation. In addition, our contour parameterization enables multi-scale segmentation that considerably

increases accuracy and segmentation speed.

We have applied our method to 20MHz IVUS images. However, on higher-frequency IVUS images (i.e., 30-40 MHz) the speckle noise will be higher making it difficult to segment using our method since we employ only grey-level histograms to compute the likelihoods. We could model the speckle intensities using the Rayleigh distribution [6] or estimate the grey-levels distributions using a mixture of Gaussians. However, we believe that by incorporating texture features in our *a priori* information [3], we will obtain more accurate likelihoods that would lead to a successful segmentation on high-frequency IVUS images.

We have not applied our method for the identification of the media/adventita border. However, since the media is observed as a thin black line and the adventitia tissue appears very bright because of its echogenic characteristics [17], we believe that the same formulation will work to segment the media/adventita contour. This can be accomplished by combining pixel intensities with image-gradient information [10] on the *a priori* information (i.e., likelihoods) with some minor modifications to our segmentation method. Variable width Gaussians, prior detection of side branches and preprocessing of the image (i.e., modified intensity [17]) will be examined in future work.

Aknowledgments: This work was supported in part by CONACYT and CONCYTEG (Mexico) under Grants 61367 and 06-02-K117-95-A02, respectively. Mendizabal-Ruiz was supported in part by scholarships from CONACYT and CIMAT. I.A. Kakadiaris was supported in part by NSF Grant IIS-0431144. Any opinions, findings, conclusions or recommendations expressed in this material are of the authors and may not reflect the views of the sponsors.

References

[1] J. Bland and D. Altman. Statistical methods for assessing agreement between two methods of clinical measurement. *Lancet*, 1:307–310, 1986. 6

[2] E. Brusseau and C. de Korte. Fully automatic luminal contour segmentation in intracoronary ultrasound imaging - a statistical approach. *IEEE Transactions on Medical Imaging*, 2004. 1

[3] E. dos Santos Filho, M. Yoshizawa, A. Tanaka, and Y. Saijo. A study on intravascular ultrasound image processing. *Record of Electrical and Communication Engineering Conversazione, Tohoku University*, 74(2):30–33, 2006. 8

[4] D. Gil, A. Hernandez, O. Rodriguez, J. Mauri, and P. Radeva. Statistical strategy for anisotropic adventitia modelling in IVUS. *IEEE Transactions on Medical Imaging*, 25(6):768–778, 2006. 2

[5] D. Gil, P. Radeva, J. Saludes, and J. Mauri. Automatic segmentation of artery wall in coronary IVUS images: a probabilistic approach. *Proc. Computers in Cardiology*, pages 687–690, 2000. 2

[6] D. Guo. Intravascular ultrasound speckle statistics. In *Proc. IEEE Engineering in Medicine and Biology Society*, pages 796–799, 1998. 8

[7] C. Haas, H. Ermert, S. Holt, P. Grewe, A. Machraoui, and J. Barmeyer. Segmentation of 3D intravascular ultrasonic images based on a random field model. *Ultrasound in Medicine and Biology*, 26(2):297–306, 2000. 1

[8] J. Kim, J. Fisher III, A. Yezzi, M. Cetin, and A. Willsky. A nonparametric statistical method for image segmentation using information theory and curve evolution. *IEEE Transactions on Image Processing*, 14(10):1486–1502, 2005. 1

[9] J. D. Klingensmith, R. Shekhar, and D. G. Vince. Evaluation of three-dimensional segmentation algorithms for the identification of luminal and medial-adventitial borders in intravascular ultrasound images. *IEEE Transactions on Medical Imaging*, 19(10):996–110, Oct 2000. 1

[10] G. Kovalski, R. Beyar, R. Shofti, and H. Azhari. Three-dimensional automatic quantitative analysis of intravascular ultrasound images. *Ultrasound in Medicine and Biology*, 26(4):527–537, 2000. 1, 8

[11] A. Mojsilovic, M. Popovic, N. Amodaj, R. Babic, and M. Ostojic. Automatic segmentation of intravascular ultrasound images: a texture-based approach. *Annals of Biomedical Enginering*, 25(6):1059–1071, 1997. 1

[12] J. Nocedal and S. Wright. *Numerical Optimization*. Springer, 1999. 3, 4

[13] S. M. O'Malley, M. Naghavi, and I. A. Kakadiaris. One-class acoustic characterization applied to blood detection in IVUS. *Proc. of the 10th International Conference on Medical Image Computing and Computer Assisted Intervention (MICCAI), Brisbane, Australia, October 2007.* 1

[14] M. Rivera, O. Ocegueda, and J. L. Marroquin. Entropy-controlled quadratic Markov measure field models for efficient image segmentation. *IEEE Transactions on Image Processing*, 8(12):3047–3057, Dec. 2007. 1, 3

[15] M. Sonka and X. Zhang. Segmentation of intravascular ultrasound images: A knowledge-based approach. *IEEE Transactions on Medical Imaging*, 14:719–732, 1995. 1

[16] J. Udupa, Y. Jin, C. Imielinska, A. Laine, W. Shen, and S. Heymsfield. Segmentation and evaluation of adipose tissue from whole body MRI scans. In *Proc. of the 6th International Conference on Medical Image Computing and Computer-Assisted Intervention, Montreal, Canada, November 15-18*, pages 635–642, 2003. 6

[17] G. Unal, S. Bucher, S. Carlier, G. Slabaugh, T. Fang, and K. Tanaka. Shape-driven segmentation of intravascular ultrasound images. In *Proc. of the International Workshop on Computer Vision for Intravascular Imaging (CVII), MICCAI, Copenhagen, Denmark*, 2006. 2, 8

[18] C. von Birgelen, C. D. Mario, W. Li, J. C. H. Schuurbiers, C. J. Slager, P. J. de Feyter, P. W. Serruys, and J. R. T. C. Roelandt. Morphometric analysis in three-dimensional intracoronary ultrasound: an in vitro and in vivo study using a novel system for the contour detection of lumen and plaque. *American Heart Journal*, 132(2):516–527, 1996. 1

[19] X. Zhang, C. R. McKay, and M. Sonka. Tissue characterization in intravascular ultrasound images. *IEEE Transactions on Medical Imaging*, 17(6):889–899, Dec 1998. 1